ARTICLE

Gold/ultra-high molecular weight polyethylene nanocomposites for electrical energy storage: Enhanced recovery efficiency upon uniaxial deformation

Stavros X. Drakopoulos[1] | Georgia C. Manika[2] | Aurora Nogales[3] |
Taeyong Kim[4] | Andrew B. Robbins[4] | Gianfranco Claudio[5] |
Austin J. Minnich[4] | Tiberio A. Ezquerra[3] | Georgios C. Psarras[2] |
Ignacio Martin-Fabiani[1] | Sara Ronca[1]

[1]Department of Materials, Loughborough University, England, UK

[2]Smart Materials & Nanodielectrics Laboratory, Department of Materials Science, University of Patras, Patras, Greece

[3]Macromolecular Physics Department, Instituto de Estructura de la Materia (IEM-CSIC), Serrano, Spain

[4]Division of Engineering and Applied Science, California Institute of Technology, Pasadena, California, USA

[5]Centre for Renewable Energy Systems Technology, Wolfson School of Mechanical, Electrical and Manufacturing Engineering, Loughborough University, England, UK

Correspondence
Stavros X. Drakopoulos, Department of Materials, Loughborough University, Leicestershire LE11 3TU, England, UK.
Email: s.x.drakopoulos@bham.ac.uk

Funding information
Engineering and Physical Sciences Research Council, Grant/Award Number: EP/K034405/1

Abstract

The growing demand for renewable energy sources has prompted the development of dielectric materials with the ability to store and efficiently recover electrical energy. Here, we correlate the structure and thermal conductivity of uniaxially oriented disentangled ultra-high molecular weight polyethylene (dis-UHMWPE) composites reinforced with gold nanoparticles with their electrical properties and potential application as electrical energy storage devices. Stretching increases the orientation of the polymer chains and thus the crystallinity and reduces the aggregation of gold nanoparticles while the thermal conductivity enhances significantly along the orientation axis. The structural changes driven by stretching result in two competing effects; on the one hand, the crystallinity increase reduces the permittivity of the composites and increases the resistivity, while on the other hand the recovery efficiency of oriented materials excels that of unstretched samples by up to 6 times at 5 s. Therefore, our work shows the structure–property relationship in electrical energy storage materials.

KEYWORDS

dielectric properties, energy storage, nanocomposites, polyolefins, thermal properties

1 | INTRODUCTION

The demanding societal and economic need for a diverse energy portfolio has recently driven fast progress in electrical energy storage materials and devices.[1–3] These devices find applications in modern electronic and electrical applications such as stationary power systems for hybrid and electrical vehicles, high frequency inverters for solar panels and even artificial muscles and actuators.[4,5] Upon the application of an electric field, the atomic and

molecular charges in the material move from their equilibrium positions inducing polarization.[6] In linear dielectric materials, where the polarization is proportional to the applied electric field, the energy stored per unit volume increases when permittivity increases.[7,8] Therefore, an ideal electrical energy storage material would exhibit high permittivity, high dielectric breakdown strength (the highest electric field that a dielectric material can withstand without breaking) and low energy losses (heat loss due to dipoles' re-orientation which leads to a reduction of the efficiency of a dielectric material).[8–10]

The use of polymers for electrical energy storage would offer advantages in terms of mechanical, lightweight, processing, and insulating properties but their dielectric permittivity is significantly low, thus decreasing their ability to store energy.[11–14] However, ferroelectric polymers and polysaccharides with relatively high dielectric permittivity values (exceeding 10) have been the subject of intense research investigation, as novel polymer dielectrics matrices with better electrical properties.[15–17] In either case, nanofillers of various shapes and electrical characteristics have been introduced to enhance the dielectric properties of polymers.[18] The addition of high-permittivity, wide bandgap nanofillers in polymers has been reported to enhance voltage endurance and their breakdown strength.[19,20] The breakdown strength in particularly can be reinforced further by orienting the fillers or the crystallites by optimizing the electric field distribution inside the nanocomposites and changing the breakdown tree inception and propagation across the dielectric medium.[21,22] The crystallites' orientation is one of the main reasons why biaxially oriented polypropylene is the material of choice for film capacitors in power system applications.[23,24]

In nanocomposites where the electrical characteristics of the filler (permittivity and conductivity) are vastly different from that of the matrix (e.g. conductive nanoparticles in a dielectric polymer), the dielectric properties are dominated by interfacial phenomena.[25,26] These interfacial phenomena are caused by physical and/or chemical interactions between polymer-nanoparticle or nanoparticle-nanoparticle interactions.[27] However, the smaller the dimensions of the nanoparticles the higher is their surface area, which leads to a much higher tendency to aggregate in order to decrease their surface energy.[28] For this reason, surface treatment and functionalization by chemical means is often employed to avoid aggregation.[29] Different materials have been employed as nanofillers in polymer energy nanocomposites, such as ceramic particles with ferroelectric properties like $BaTiO_3$,[30] 2D nanomaterials like boron nitride,[31,32] and various carbon allotropes.[33,34] Conductive materials below the percolation threshold, have been used as nanofillers in the past to improve the dielectric response, reduce the

dielectric loss, and increase the recoverable energy storage, targeting the optimum compromise between the enhancement of dielectric constant[35] and the reduction of the dielectric breakdown strength.[36]

Another limiting factor of the use of amorphous polymers in electrical applications is their tendency to build up heat, as a result of their generally low thermal conductivities (0.1 to 1.0 Wm^{-1} K^{-1}[37,38]). Over the past decades, there has been a growing interest in the synthesis of ultra-high molecular weight polyethylene (UHMWPE), with an average molecular weight above 10^6 g/mol.[39] We reported that UHMWPE with reduced number of entanglements (dis-UHMWPE) can be synthesized by using a single-site homogenous catalytic system, improving its processing ability[40] and thermo-mechanical properties,[41] when compared to the highly entangled samples commonly obtained with Ziegler-Natta catalysts. The use of tensile stretching to fabricate highly oriented tapes results in improved mechanical and thermal properties,[42] with some of them reaching metallic-like thermal conductivities.[43] Enhancement upon the thermal conductivity of dielectric materials is required to secure the thermal stability of the electronic components due to the fast distribution of heat generated by the electric current. We recently explained this phenomenon on the basis of ballistic phonons traveling distances as far as 200 nm and traversing crystalline domains via transient grating spectroscopy.[44] The combination of high thermal conductivity, electrical insulation, ultra-high molecular weight, and light weight makes oriented dis-UHMWPE an ideal candidate for a matrix material in an electric energy storage composite.[45,46] In addition, unstretched dis-UHMWPE samples exhibit significantly higher or similar crystallinities (70%) comparing to biaxially oriented polypropylene (45%–70%),[23,24] contributing to the notion that dis-UHMWPE nanocomposites can be suitable dielectric materials with high breakdown strength, especially after orientation than can increase crystallinity up to 90%.[45,47] Up to now, the use of gold nanoparticles as reinforcing fillers in oriented UHMWPE has been limited to studies of the optical/dichroic properties[48] and biomedical imaging.[49] Interestingly, the degree of orientation in dis-UHMWPE upon the formation of entanglements works in an equivalent way as with molecular weight even in the melt state; the higher the pre-melt draw ratio, the stronger the hindering effect in the formation of entanglements.[50]

In this work, we have prepared nanocomposites of gold nanoparticles and UHMWPE, and uniaxially stretched them to low drawing ratios. We present a thorough structural study on the crystallinity and orientation induced by stretching and by means of wide and small angle x-ray scattering (WAXS/SAXS), Raman, and

near infrared spectroscopy. We study the effect of stretching on the thermal properties of the composites through the measurement of their thermal conductivities at varying angles with respect of the chain orientation. Then, we harness these insights to prove the application of the composites as electrical energy storage devices, placing an emphasis on how to optimize the energy recovery from the charged system. Our work shows how oriented gold/polyethylene nanocomposites can provide a pathway towards thinner, lighter, more efficient, and thermally stable capacitors for energy storage applications.

2 | EXPERIMENTAL

2.1 | Materials

The synthesis of dis-UHMWPE was performed in-house according to the procedure described elsewhere.[51] The polymerization reaction was quenched with acidified methanol (methanol (CH_3OH)/37% w/w hydrochloric acid (HCl) 95/5 v/v) to completely avoid the formation of aluminum oxide (Al_2O_3) catalytic ashes from the methyaluminoxane (MAO) co-catalyst used. Since acidic methanol was employed for quenching the chemical synthesis, our specimens do not contain any Al_2O_3 catalytic ashes, which can work as dielectric probes by increasing the dielectric relazation strength as reported in the literature.[52,53] The average molecular weight was determined by rheological measurements as $M_w = 5.6 \times 10^6$ g/mol.[54] Dodecanethiol functionalized Au nanoparticles (2–5 nm in diameter) in toluene (2% w/v) were purchased by Sigma-Aldrich and used as received. Although the functionalized Au nanoparticles cannot work as dielectric probes, they are expected to enhance significantly the interfacial polarization phenomena within the insulating polymer matrix due to the vastly higher electrical conductivity that they introduce within polyethylene.[55]

2.2 | Sample preparation

To prepare dis-UHMWPE nanocomposites modified with dodecanethiol functionalized gold (Au) nanoparticles, dis-UHMWPE in powder form was suspended in acetone (C_3H_6O) and toluene (C_7H_8) solutions of nanoparticles were added under magnetic stirring. The stirring was maintained for few hours and then the solvent evaporated under a fume hood overnight. Complete removal of residual solvent was achieved by heating the composites to 50°C in a vacuum oven for 6 h. As investigated in similar systems, this temperature is below the activation temperature of the formation of entanglements (58°C).[52] In

this study, the effect of draw ratio is investigated thus, the dodecanethiol functionalized Au nanoparticles concentration in dis-UHMWPE was kept constant at 1.0% w/w. Au nanoparticles were chosen as a nanofiller for their very high electrical conductivity and anticorrosive characteristics. Variation of the electrical energy storage properties as a function of the fillers' concentration is going to be investigated in the future. The resulting powder was compression-molded in an hydraulic press at 125°C using the protocol described elsewhere.[52] Unstretched samples were prepared in the form of two cylindrical discs of 25 mm in diameter and 1.1 mm in thickness. Samples for stretching were prepared as square films of 5 × 6 mm with an initial thickness of 1.9 mm. The square samples were submitted to uniaxial deformation to reach drawing ratios (DR) from 1 to 5 via a twin-roll mill at 125°C.

2.3 | Characterization

2.3.1 | Wide-angle X-ray scattering

Wide angle X-ray scattering (WAXS) experiments were carried out in a diffractometer Policristal X'Pert Pro PANalytical working in a θ-2θ configuration using the Cu Kα wavelength.

2.3.2 | Transmission electron microscopy

The samples were cut using cryo-sectioning and resin embedding. For cryo-sectioning both samples were cut at −100°C for 70 nm thick sections and −105°C for 50 nm sections, using a cryo-diamond knife. Sections were collected onto holey carbon 300 mesh Cu grids using the sucrose pick up method and washed with sterile water to return to room temperature and blotted dry on filter paper. Resin used was Agar Low Viscosity Resin, polymerized for 48 h at 60°C. The 50 and 70 nm sections were cut with a diamond knife and sections collected onto either holey carbon grids as before, or 400 mesh plain Cu grids & air dried. The TEM measurements were performed using JEOL 2100Plus operated at 80 kV.

2.3.3 | Small-angle X-ray scattering

Small-angle X-ray scattering (SAXS) experiments were carried out on a Bruker AXS Nanostar small-angle X-ray scattering instrument. The instrument uses Cu Kα radiation (1.54 Å) produced in a sealed tube. The scattered X-rays are detected on a two-dimensional multiwire area

detector (Hi-star, Bruker) and can be converted to one-dimensional scattering by radial averaging and represented as a function of momentum transfer vector q ($q = 4\pi \sin \theta/\lambda$) in which θ is half the scattering angle and λ is the wavelength of the incident X-ray beam. The sample to detector distance was 106 cm. The scattered intensity was corrected with the transmission of the samples calculated considering the absorption of the sample. A glassy carbon standard was used for this purpose.

2.3.4 | Raman spectroscopy

The Raman spectra of the samples were analyzed in the wavenumber range of 1500 to 1000 cm^{-1} at room temperature employing a laser beam at 633 nm. The Raman system used was a LabRAM HR provided by Horiba Jobin-Yvon (France).

2.3.5 | Vis/NIR spectrophotometer

The absorption of the samples was investigated in the visible wavelength range of 400 to 750 nm and at the near infra-red wavelength of 950 to 1800 nm at room temperature. The apparatus employed was a Cary 5000 UV–Vis–NIR spectrophotometer from Agilent Technologies (Santa Clara, CA).

2.3.6 | Transient grating spectroscopy

The thermal conductivities of the samples were measured using transient grating spectroscopy at 30°C. The technique is adapted following prior works.[44,56,57] Briefly, a pair of pump pulses (wavelength 515 nm, pulse duration ~1.0 ns, pulse energy ~13 µJ, repetition rate 200 Hz) is focused onto the sample to create a spatially periodic heating profile that yields transient thermal grating (grating period ~10.7 um). A pair of continuous wave laser beams (wavelength 532 nm, average power ~27 mW, chopped at 3.4% duty cycle to minimize steady heating) diffracts from the thermal grating, monitoring its relaxation. We employ heterodyne detection method in which we measure the coherent interference of the diffracted probe beam and a reference beam, thereby significantly increasing signal-to-noise ratio.

2.3.7 | Dielectric spectroscopy

The samples were studied by means of dielectric spectroscopy employing an Alpha-N Frequency Response Analyzer, with a constant V_{rms} of 3 V and frequency varying from 10^{-2} to 10^3 Hz at 30°C. A second set of measurements was performed in the frequency range of 10^0 to 10^3 Hz and temperature range of 50 to 160°C with a step of 10°C to evaluate the thermal stability, and presented in Figure S4. The analysis was limited to frequencies up to 10^3 Hz because at higher frequencies, the values of $\tan\delta = \varepsilon''/\varepsilon'$ are very close to the limits of detection of the frequency analyzer, resulting in increased measurement error. The temperature was controlled using a Novotherm system and the dielectric test cell used was a two parallel gold-plated electrode capacitor BDS-1200, all supplied by Novocontrol Technologies (Hundsagen, Germany). The two parallel electrodes had diameters at 10 and 40 mm, respectively, resulting into an effective electrode area of 78.54 mm^2. The thicknesses of each cell are provided in the Table S1.

2.3.8 | Direct current measurements

The experiments were carried out using a 4339B High-Resistance Meter, DC provided by Agilent Technologies (Santa Clara, CA). An automatic measurement process is included in the experimental apparatus to record the charging and discharging electric current. A two parallel-plate electrodes apparatus was used with the sample lying in between throughout the experiment. Three different voltages were applied: 100, 300, and 500 V at a charging time of 60 s. It should be noted that before every experimental measurement, a discharge and short-circuit procedure was performed to avoid the accumulation of charges. To calculate the stored and recovered energy, the capacitance was recorded from dielectric measurements at the lowest measured frequency (0.01 Hz), when the dielectric permittivity is closer to the dielectric constant of the material.[58]

3 | RESULTS AND DISCUSSION

3.1 | Structural characterization

In order to appreciate the effect that stretching has on the crystalline structure of UHMWPE, wide-angle X-ray scattering (WAXS) experiments were performed. Figure 1 shows the scattered intensity of the composites as a function of the angle between the incident beam and the detector (2θ), with the peaks indexed according to the reported orthorhombic crystal structure of PE.[59] The crystallinity was calculated by dividing the area below the crystalline peaks, fitted by Lorentzian curves, by the total area of crystalline and amorphous halos. As
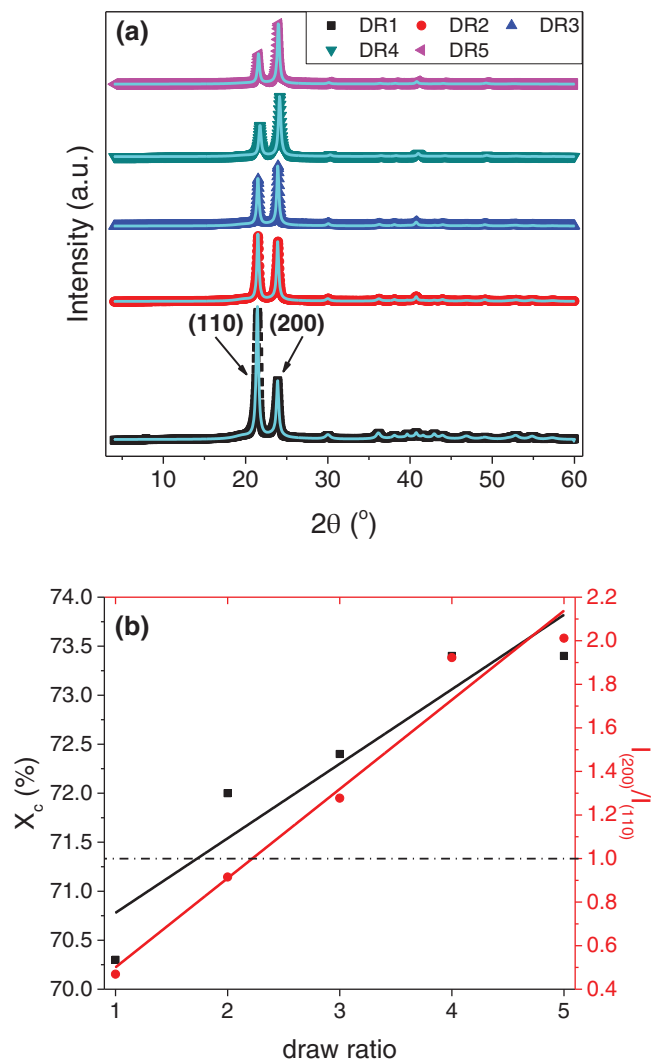
FIGURE 1 (a) WAXS profiles of gold/UHMWPE nanocomposite films where the intensity is normalized with the (200) reflection. (b) Crystallinity as calculated by WAXS (left axis) and intensity ratio of the (200) and (110) reflections (right axis) versus draw ratio. The dotted line is a guide for the eye to show when the peak inversion of the reflections takes place [Color figure can be viewed at wileyonlinelibrary.com]

associated with planes perpendicular to the stretching direction, is a clear indication of an increase in chain orientation.

Transmission Electron Microscopy (TEM) enabled the visualization of the gold nanoparticles and aggregates in the polymer matrix, as shown in Figure 2 for an unstretched and a DR5 sample. The general trend observed is a reduction in aggregate size in the stretched sample (DR 5). Because of the challenges involved in microtoming polyethylene samples, which could alter their morphology during the process due to their softness, it is difficult to extract definite conclusions. However, in the rest of this section we present results obtained by other techniques that support this observation.

Small-angle X-ray scattering (SAXS) experiments were carried out to elucidate the crystalline structure of the composite and the gold nanoparticle distribution. Figure 3 shows the corresponding 1D profiles, normalized by the thickness of the specimens. For comparison purposes, an unstretched (DR 1) sample without Au nanoparticles has been included in the analysis.

In the absence of Au nanoparticles, two bumps are visible. The first bump is at $q = 0.29$ nm^{-1} ($L = 2\pi/q = 22$ nm) and corresponds to the long spacing of polyethylene crystalline lamellae.[60] The second bump is at around $q = 0.80$ nm^{-1} and is attributed to a second order maximum of the same long spacing.[61] The peak at $q = 0.80$ nm^{-1} is still visible when Au nanoparticles are added, while the peak at $q = 0.29$ nm^{-1} is masked by a rising low q contribution attributed to the presence of gold nanoparticle aggregates. The slope of I(q) can be fitted as $q^{-3.09}$, indicating that the aggregates are compact and scatter in a similar way as surface fractals.[62] By using the Guinier law, (Figure S1 and Table S2) the average size of the nanoparticles was found to be around 6.8 nm for all nanocomposites.

The Raman spectra of the composites is presented in Figure 4(a). The main features, observed in the 1500 to 1000 cm^{-1} region, correspond with those reported in the literature for polyethylene,[63,64] that is, skeletal C—C stretching vibrations (1130 and 1063 cm^{-1})[65] and the twisting vibration of CH$_2$ (1297 cm^{-1}). For highly crystalline samples, a contribution from the amorphous component at 1303 cm^{-1} is not observed.[66] The CH$_2$ bending vibrational mode is split into two components at 1440 and 1417 cm^{-1} which is indicative of an orthorhombic crystal structure, in accordance to our WAXS analysis.[67] In the 1400 to 1500 cm^{-1} range, the intensities of the peaks vary as a function of uniaxial stretching plastic deformation. For the case of the two amorphous peaks, 1463 and 1440 cm^{-1}, the intensity decreases, while for the 1417 cm^{-1} crystalline peak, the intensity increases as a function of stretching. The trend of the peaks is an

shown in Figure 1(b), Uniaxial stretching results in a moderate increase in crystallinity as a consequence of the enhanced chain orientation, however limited due to the low drawing ratios used. Higher drawing ratios can be achieved with further orientation with tensile stretching and are going to be explored in a future study. Another prominent feature of the WAXS profile (Figure 1(a)) is that as samples are stretched further, there is an inversion in the ratio between the (110) and (200) reflections (Figure 1(a)). This inversion can be better visualized in Figure 1(b), where the ratio switches from below to above 1 between DR2 and DR3. The prevalence of the (200) reflection at higher drawing ratios,

(a)   (b)

0.5 μm   0.5 μm
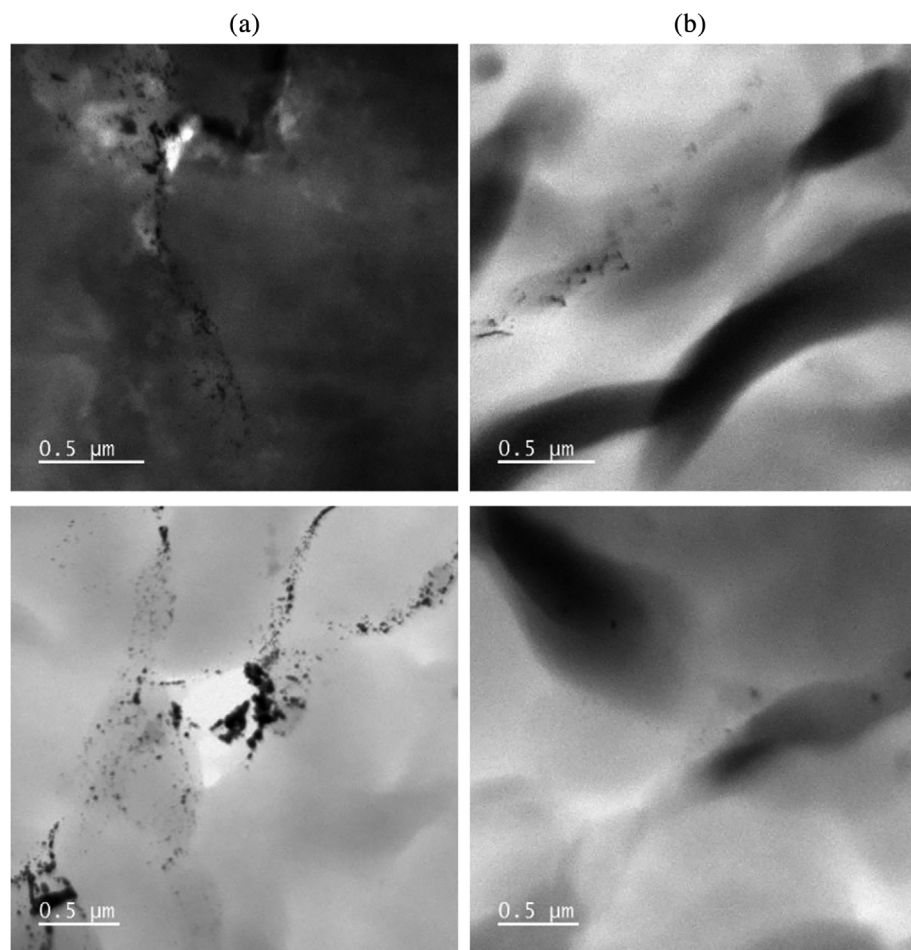
0.5 μm   0.5 μm

FIGURE 2 TEM images of the gold/UHMWPE composites (a) before stretching, and (b) uniaxially stretched up to a draw ratio of 5 (DR 5)
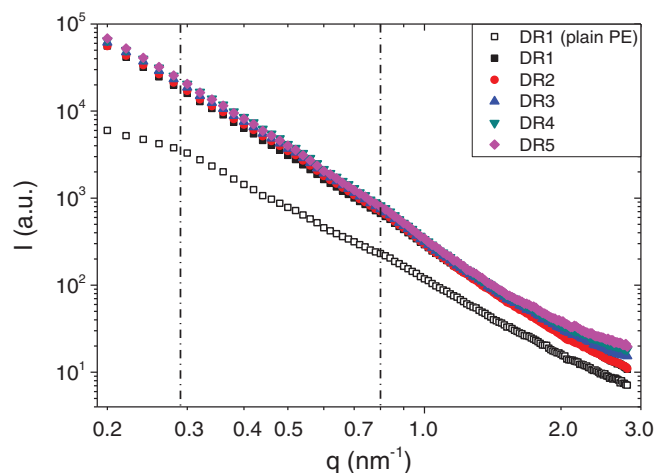

FIGURE 3 SAXS profile of gold/UHMWPE nanocomposite films normalized by the thickness for all samples under study including the DR 1 in the absence of au nanoparticles [Color figure can be viewed at wileyonlinelibrary.com]

indirect way to show that the crystallinity increases upon stretching, in agreement with the WAXS experiments. These data can be appreciated further in Figure S2 and Table SI3 and Table SI4.

To further elucidate the structure of the composites, visible and near infrared (Vis/NIR) spectra were acquired and presented in Figure 4(b). In the visible part of the spectrum, the peak at 539 nm is associated with the transverse plasmon resonance of the Au nanoparticles.[68] For the DR 1 (unstretched) and DR 2 samples, the peak is broad, indicating gold nanoparticles of different sizes or aggregates. At the highest drawing ratios investigated (DR 4 and DR 5) the peak is more intense and narrower, an indication that some of the clusters are breaking apart due to the progressive orientation of the chains.

In the near infrared region, the main contribution to the absorbance is expected to come from the polymer matrix, as no absorption is expected from the Au nanoparticles.[68] The peak at 1731 nm, associated with the antisymmetric stretching mode of CH_2 group in crystals, becomes more intense as stretching proceeds. This is a clear signature of orientation, as this mode has its electric dipole-transition moment perpendicular to the polymer backbone.[69] The peaks at 1215, 1432, and 1764 nm are slightly affected by orientation as well; the latter is also related with the crystalline phase, while the peak at 1215 nm has been reported to increase with the increase in

(a)

(b)
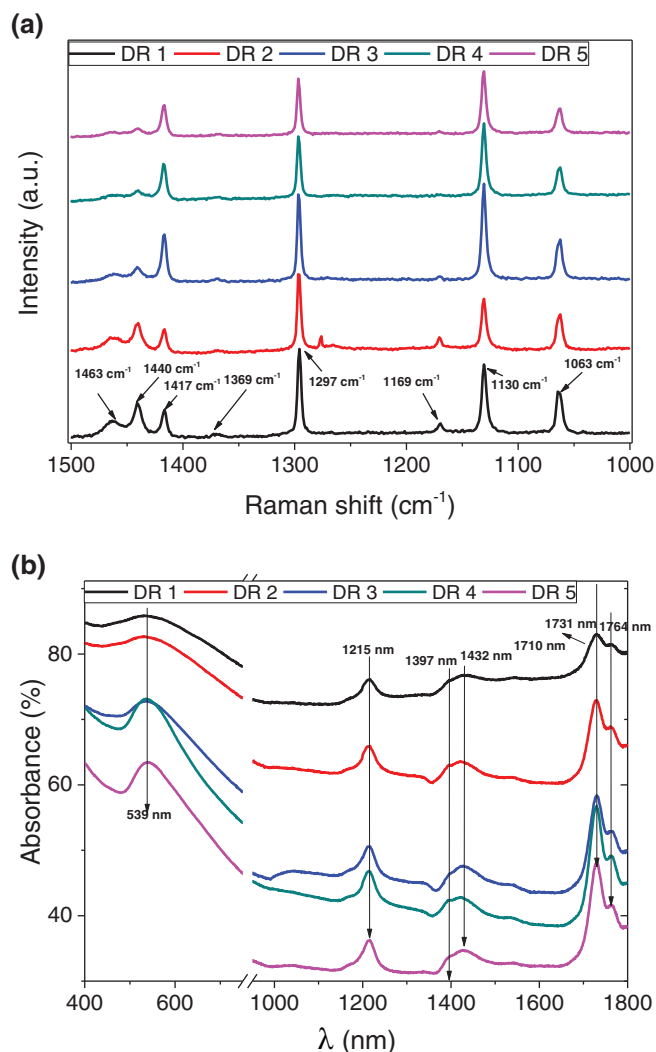
FIGURE 4 (a) Raman spectra as a function of wavenumber and (b) Vis/NIR absorbance as a function of wavelength at room temperature varying the draw ratio for gold/UHMWPE nanocomposite films [Color figure can be viewed at wileyonlinelibrary.com]

density.[70] In our experiments, density is expected to increase with the increase of order (either higher crystalline percentage or induced order in the amorphous regions) and it can be associated with this slight increase that we observed over stretching deformation. A very small shoulder at 1710 nm is indicating a peak, which is present only in the unstretched sample. This peak is associated with the amorphous component and its disappearance only strengthens the notion that the crystallinity and oriented amorphous components increase with stretching.[69,71]

3.2 | Thermal conductivity

Enhanced thermal conductivity is desired in electrical storage devices, to avoid overheating and minimize safety
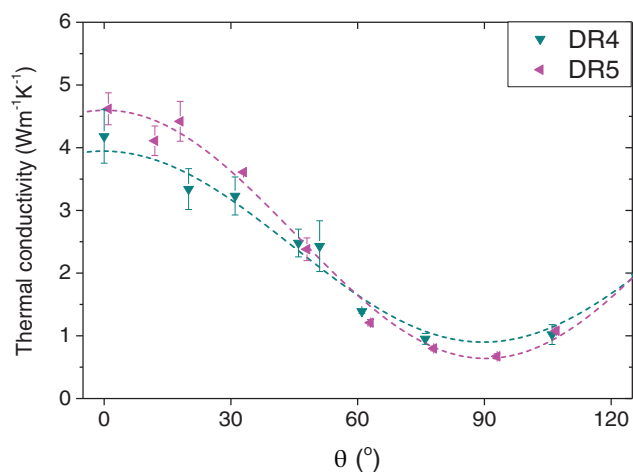
FIGURE 5 Measured thermal conductivity for partially drawn gold/UHMWPE nanocomposite films (DR4 and DR5) versus the angle with respect to the stretching direction at 30°C [Color figure can be viewed at wileyonlinelibrary.com]

concerns.[72] To assess the influence of stretching and to study how the oriented chains improve the thermal transport along the chain direction ($\theta = 0°$) compared to that along the perpendicular direction ($\theta = 90°$), we studied the in-plane thermal conductivity as a function of the rotation angle. DR4 and DR5 were the only samples that could be measured with transient grating spectroscopy, as the lower DR specimens would scatter too strongly. Figure 5 shows their angle-dependent thermal conductivity, which peaks at $\theta = 0°$: 4.2 ± 0.4 Wm^{-1} K^{-1} for DR4, and 4.6 ± 0.4 Wm^{-1} K^{-1} for DR5. These are significantly higher thermal conductivities than those reported in the literature for unstretched UHMWPE, namely ~ 0.3 Wm^{-1} K^{-1}.[43] This drastic enhancement in thermal conductivity, even at low draw ratios as investigated here, is a result of the crystalline and amorphous segments orientation, small crystallinity growth, and phonon propagation with mean free paths that sometimes exceed the crystal size. These ballistic phonons contribute to nearly one third of the overall thermal conductivity, as we have investigated in a previous study.[44] The effect that gold nanoparticles have upon the thermal conductivity values is considered negligible since very similar thermal conductivity values were obtained from other dis-UHMWPE nanocomposites studied with thermal grating spectroscopy[44] and plain dis-UHMWPE studied with laser-flash thermal analysis[43] for DR5. At higher draw ratio when the crystallinity increases significantly, reaching values close to 90%, the thermal conductivities exceed 50 Wm^{-1} K^{-1}.[43] We fit the results to the geometrical model based on the measured principal in-plane thermal conductivity values and find good agreement.[44] The fitted anisotropy ratio of the thermal transport along the chain

(a)

(b)
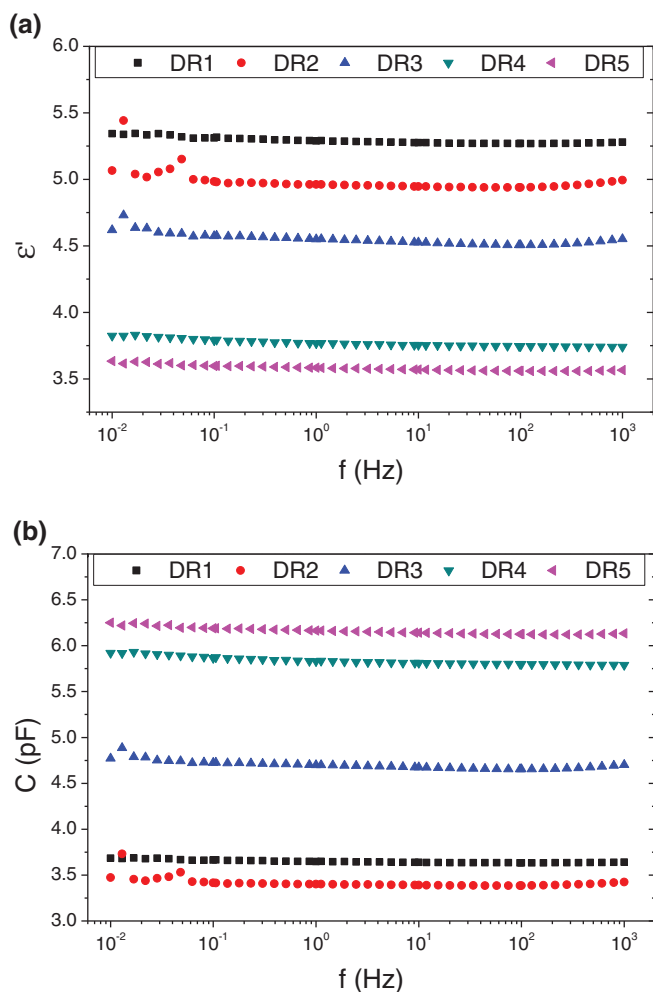
FIGURE 6 (a) The real part of dielectric permittivity and (b) the capacitance as a function of frequency at 30°C varying the stretching draw ratio of the gold/UHMWPE nanocomposite films [Color figure can be viewed at wileyonlinelibrary.com]

direction to perpendicular direction for the DR4 and DR5 samples is 4, and 7, respectively. We note the peak of the thermal conductivity increases with the draw ratio while its minimum decreases, indicating an increase in thermal anisotropy with draw ratio and therefore an improved heat dissipation along the orientation axis.

3.3 | Electrical energy storage application

Because of the combination of a dielectric matrix with a conducting nanofiller, as well as their enhanced thermal conductivity and light weight, our uniaxially stretched UHMWPE/gold nanocomposites are excellent candidates for electrical energy storage devices. To test their application as dielectric capacitors, first the dielectric behavior of the samples was measured as a function of the external

electric field frequency at 30°C, as presented in Figure 6. The dielectric formalism employed in this work is the complex dielectric permittivity, which is a good measure of the uniaxial orientation as it is independent of the thickness of the capacitor for thicknesses that correspond to the bulk properties of the materials like in this case. The complex dielectric permittivity follows the Equation 1 below:

$$\varepsilon^* = \varepsilon' - i\varepsilon'' \tag{1}$$

where ε' and ε'' are the real and imaginary parts of dielectric permittivity, respectively. As it can be appreciated in Figure 6(a), the real part of the dielectric permittivity exhibits a behavior that does not depend strongly on frequency, with no significant increase approaching the lower frequency edge. This corresponds to the low-loss character of plain polyethylene, which is a desirable property in energy storage materials, as it is also evident in Figure S3 where tan δ <0.02 in the studied frequency range at 30°C.

Additionally, it can be observed that the dielectric permittivity decreases for increasing drawing ratios, a phenomenon that can be correlated to the higher orientation and the increase in crystallinity proven by WAXS, Raman, and NIR spectroscopy measurements. With the orientation of the crystalline and amorphous regions, the ability of the corresponding polymer phases to be polarized is hindered, hence permittivity decreases. Finally, it can be seen that the material is thermally and dielectrically stable at elevated temperatures as high as 120°C, as depicted in Figure S4 for the DR5 sample. Even at 120°C, the loss tangent values at 10 Hz are significantly low (tan δ ≈ 0.02). At the same temperature, the loss tangent values of a plain dis-UHMWPE (DR1) are below 0.005 presented in Figure S4, hence the elevated tan δ values of the nanocomposites are due to the increased electrical conductivity from the gold nanoparticles.

The capacitance, C, and energy, E, of the capacitor relate to the dielectric material and the capacitor's geometry as follows:

$$C = \varepsilon\varepsilon_0 \frac{A}{d} \tag{2}$$

$$E = \int_0^Q Vdq = \frac{1}{2}\frac{Q^2}{C} \tag{3}$$

where ε is the static value of dielectric permittivity of the material, ε_0 the dielectric constant of free space, A and d are the electrodes' surface and distance and Q is the accumulated charge. Although the dielectric permittivity values are not dependent on the thickness of the capacitor, in Figure 6(b) it is shown that the reduction in
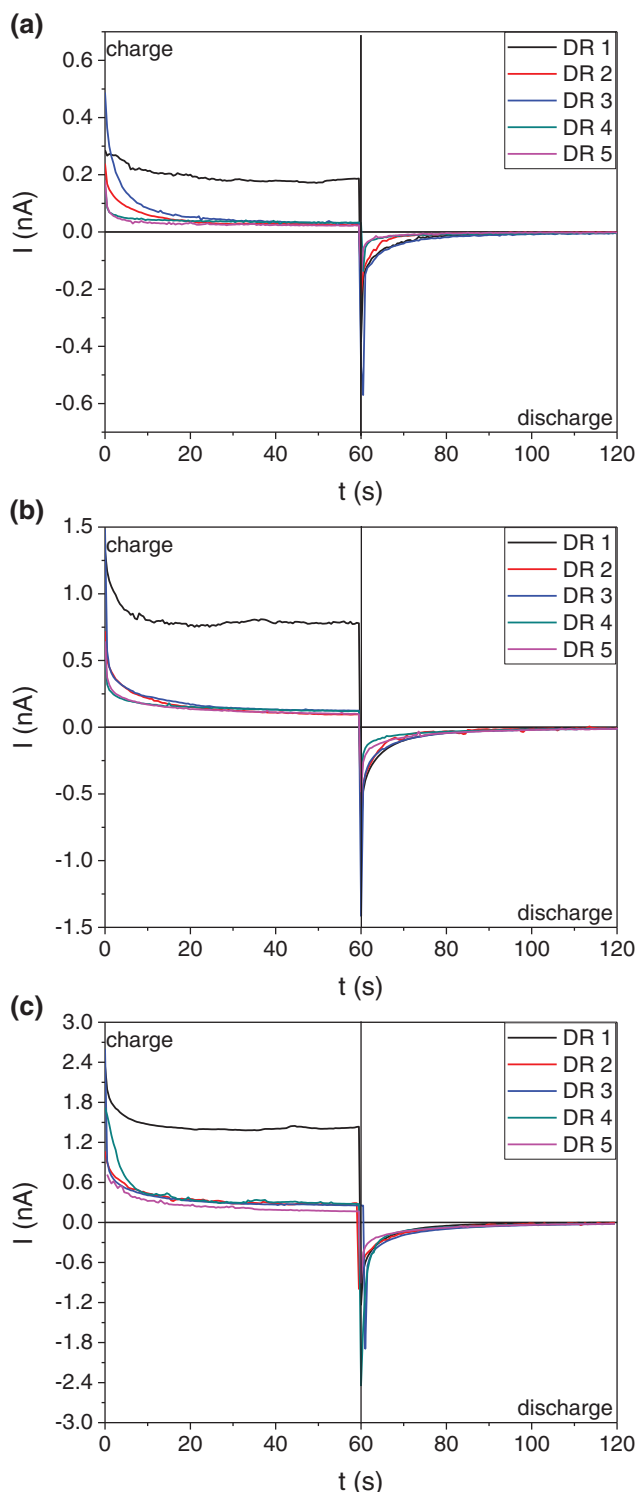
FIGURE 7 The charge–discharge dc currents gold/UHMWPE nanocomposite films as a function of time for different drawing ratios at: (a) 100, (b) 300, and (c) 500 V [Color figure can be viewed at wileyonlinelibrary.com]

thickness as a result of stretching (lowering the d value in Equation 2) has an impact on the capacitance of the system. Since the thickness of the DR 1 and DR 2 samples is very close, the capacitance is only affected by their

permittivity difference resulting in a slightly decreased value as presented in Figure 6(b).

The next step was evaluating the performance of the composites during a charge–discharge cycle. In Figure 7 the charge and discharge currents under a dc electrical field are presented for all the samples as a function of time at 100, 300, and 500 V. Firstly, the current intensity drops as the capacitor is charging until it reaches a constant value. After we stop applying the external field, the discharging process begins with an initially sharp discharge that plateaus close to zero intensity after most of the energy has been recovered. With increasing voltage, both the charge and discharge currents values increase.

Stored (E_s) and recovered (E_r) energies were calculated by integrating the charge (I_c) and discharge (I_d) currents, respectively,[30,58] as it can also be seen schematically in the Figure S5:

$$E_s = \frac{1}{2}\frac{\left[\int I_c(t)dt\right]^2}{C} \ and \ E_r = \frac{1}{2}\frac{\left[\int I_d(t)dt\right]^2}{C} \quad (4)$$

Figure 8 presents the recovered energy density as a function of time for different drawing ratios during the discharge period. As the applied voltage increases (field intensity), the energy density values enhance significantly for the samples under study as the number of charge carriers injected by the electrodes also increases, facilitating the transportation of the charges within the material by lowering the local potential barrier. This has a more pronounced effect in the higher plastic deformations (DR 4 and DR 5). At 500 V, the energy density generally increases with stretching and all the oriented samples exhibit energy density values which are at least double when compared to the unstretched one. It should be noted that the calculated energies are a slight overestimation since the dielectric permittivity at the lowest measured frequency is slightly lower than the expected dielectric constant. However, the dielectric relaxation strength of polyethylene is very low in the absence of dielectric probes as discussed earlier, and so no significant changes are expected in the static permittivity values at this temperature.

To quantify the electrical energy efficiency of the specimens under different voltages, the coefficient of recovery efficiency was calculated as[30,58]:

$$n_{eff} = \frac{E_r}{E_s}x100\% \quad (5)$$

The coefficient of recovery efficiency of the oriented samples, presented as an inset in Figure 8 (5 s) and shown in
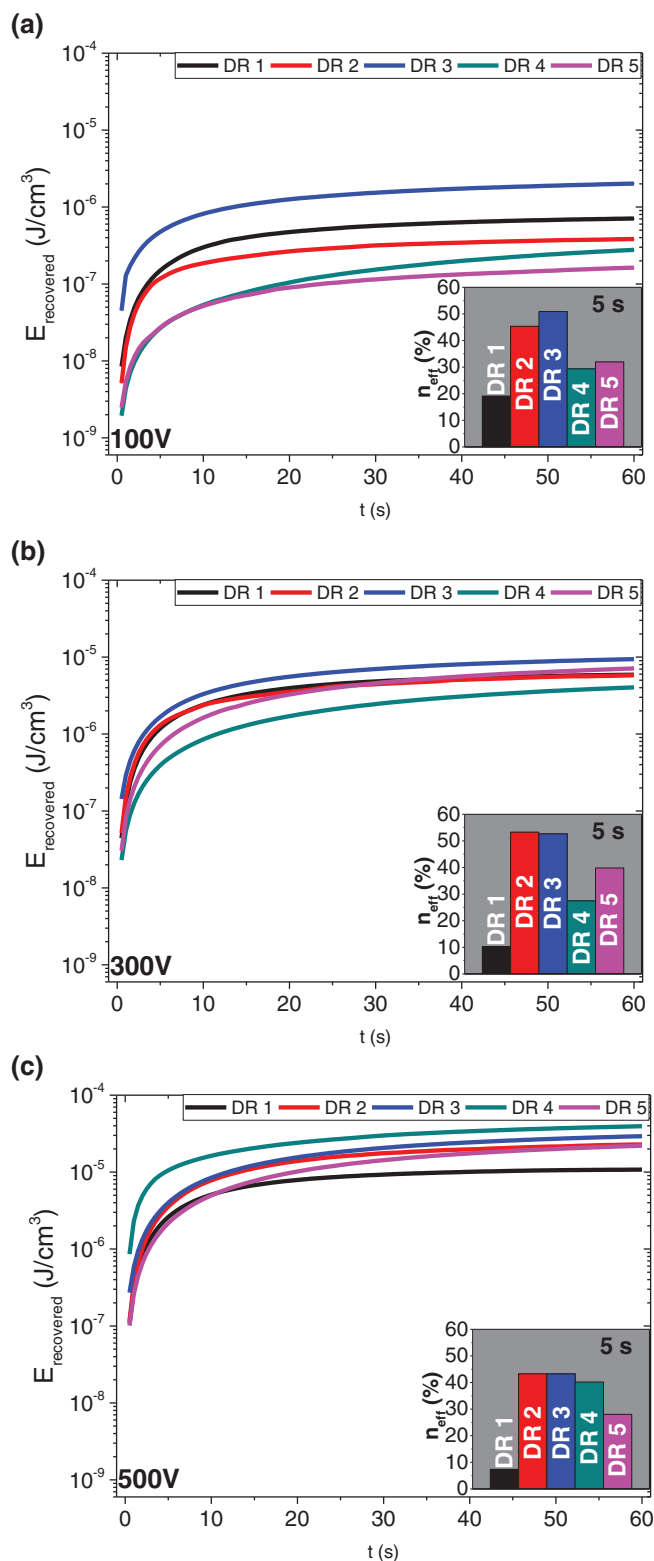
FIGURE 8 Recovered energy density values of gold/UHMWPE nanocomposite films as a function of time varying the draw ratio for: (a) 100, (b) 300, and (c) 500 V. the inset represents the coefficient of energy recovery efficiency after 5 s of discharge [Color figure can be viewed at wileyonlinelibrary.com]
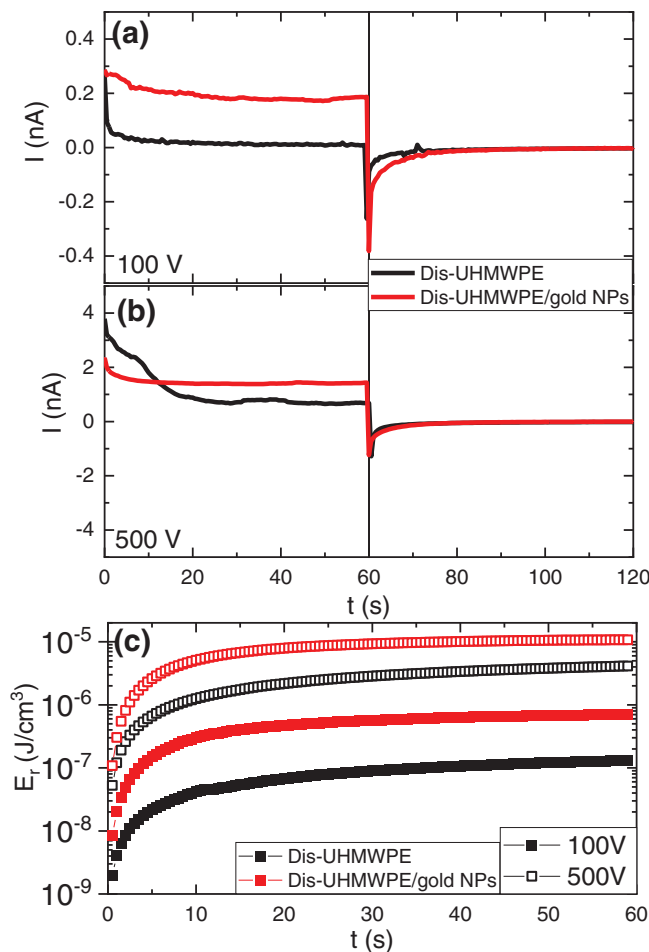
FIGURE 9 The charge–discharge dc currents of DR1 (unstretched) plain UHMWPE (black) and gold/UHMWPE (red) nanocomposite as a function of time for different drawing ratios at: (a) 100 and (b) 500 V. at (c) the recovered energy density values are presented [Color figure can be viewed at wileyonlinelibrary.com]

Figure S6 and Table S5 (30 s), is dramatically enhanced when compared to the unstretched composites. Since the efficiency is time-dependent and decreases over time (as shown Figure S6), at shorter times is considerably higher, reaching 50% for the sample DR3 at 100 V. At 5 s, the efficiency values of the oriented samples for all voltages is up to 6 times higher than that of the unstretched dis-UHMWPE nanocomposite and it is even more pronounced at longer times (as presented in Figure S6). During discharge, the recovered energy is associated with the movement of unbounded charge carriers and possibly with the formation/deformation of induced dipoles close to the surfaces of the electrodes and at the constituents′ interface. All these are related to the resistivity and the charges space distribution or concentration at the interfacial area of the nanoparticles. After uniaxial orientation we have shown earlier (Figure 1(a)) that the crystallinity

associated with the polymer increases, diminishing thus the electrical conductivity and narrowing the distribution of gold nanoparticles which in return increases the electrical conductivity and enhances the systems' heterogeneity and interfacial polarization phenomena. From the plasmon resonance of the Au nanoparticles at the visible wavelength spectrum, we observed that as stretching plastic deformation increases, the peak gets more intense due to the breaking of the clusters/aggregates. This effect should increase the contribution of interfacial phenomena between the polymer chains and the nanoparticles and possibly enhance the accumulation of charges at the interface of an insulator/conductor system due to Maxwell-Wagner-Sillars interfacial polarization phenomena.[25,50,73] Therefore, the improvement we monitor in the coefficient of recovery efficiency after stretching is attributed to the enhancement of interfacial polarization.

The comparison between DR1 plain UHMWPE and gold/UHMWPE samples as dielectric materials in a capacitor is provided in Figure 9. The charge current under a dc electrical field and the discharge current are presented as a function of time at 100 and 500 V. By integrating the area below the discharge currents following Equation (4), we obtain the recovery energy densities which strongly show that the addition of 1% w/w of gold nanoparticles, comparing to plain sample, increases values by over 5.0 times at 100 V (closed symbols) and 2.5 times at 500 V (open symbols).

4 | CONCLUSIONS

In the present work, we prepared composites of dis-UHMWPE and dodecanethiol functionalized Au nanoparticles, and uniaxially stretched them at different drawing ratios. The structural analysis by means of Raman spectroscopy, small-angle, and wide-angle X-ray scattering revealed an increase in crystallinity and orientation for increasing drawing ratios, as well as a decrease in gold nanoparticle aggregation. Uniaxial plastic deformation significantly affected the thermal conductivity in a beneficial way increasing from the reported ~ 0.3 Wm^{-1} K^{-1} of unstretched polyethylene to up to 4.6 Wm^{-1} K^{-1}, enabling faster cooling along the orientation axis. We studied the application of these composites as electrical energy storage devices by testing their performance during charge and discharge cycles and found that the recovery efficiency increased dramatically in oriented samples. We attributed this phenomenon to interfacial polarization induced by the

presence of Au nanoparticles in the dis-UHMWPE matrix, enhanced by the breaking down of the aggregates that results in higher surface area between the conducting nanoparticles and the polymer matrix. However, with orientation comes higher crystallinity, which hinders the polymer chains mobility and their ability to be polarized, reducing the permittivity of the composites and increases the electrical resistivity. Therefore, a balance between orientation and recovery efficiency has to be reached, which in our case is embodied by the nanocomposite stretched to drawing ratio 3, which yields the optimum configuration. Therefore, the results presented here are key for the design and fabrication of composites for electrical energy storage applications, providing valuable guidance on which crystallinity and orientation values should be chosen depending on the final properties that are sought. More generally, our study paves the way toward lighter, more efficient, and thermally stable dielectric capacitors based on polymer nanocomposites.

ORCID
Stavros X. Drakopoulos https://orcid.org/0000-0002-6798-0790
Aurora Nogales https://orcid.org/0000-0002-2494-3551
Tiberio A. Ezquerra https://orcid.org/0000-0001-9966-519X
Georgios C. Psarras https://orcid.org/0000-0002-0539-2838
Ignacio Martin-Fabiani https://orcid.org/0000-0002-1977-7659
Sara Ronca https://orcid.org/0000-0003-3434-6352

REFERENCES
[1] X. Huang, P. Jiang, *Adv. Mater.* **2015**, *27*, 546.
[2] J. W. Choi, D. Aurbach, *Nat. Rev. Mater.* **2016**, *1*, 2019.
[3] V. Presser, C. R. Dennison, J. Campos, K. W. Knehr, E. C. Kumbur, Y. Gogotsi, *Adv. Energy Mater.* **2012**, *2*, 895.
[4] B. Zhao, L. Jiang, X. Zeng, K. Zhang, M. M. F. Yuen, J. B. Xu, X. Z. Fu, R. Sun, C. P. Wong, *J. Mater. Chem. A* **2016**, *4*, 14595.
[5] G. C. Psarras, *Express Polym. Lett.* **2016**, *10*, 721.
[6] L. Wen, J. Chen, J. Liang, F. Li, H. M. Cheng, *Natl. Sci. Rev.* **2017**, *4*, 20.
[7] P. Jiang, X. Huang, *IEEE Trans. Dielectr. Electr. Insul.* **2017**, *24*, 6619.
[8] X. Hao, *J. Adv. Dielectr.* **2013**, *03*, 1330001.

[9] Q. Chen, Y. Shen, S. Zhang, Q. M. Zhang, *Annu. Rev. Mater. Res.* **2015**, *45*, 433.

[10] L. Zhu, Q. Wang, *Macromolecules* **2012**, *45*, 2937.

[11] X. Zhang, Y. Shen, B. Xu, Q. Zhang, L. Gu, J. Jiang, J. Ma, Y. Lin, C. W. Nan, *Adv. Mater.* **2016**, *28*, 2055.

[12] A. Mannodi-Kanakkithodi, G. M. Treich, T. D. Huan, R. Ma, M. Tefferi, Y. Cao, G. A. Sotzing, R. Ramprasad, *Adv. Mater.* **2016**, *28*, 6277.

[13] Z. Yao, Z. Song, H. Hao, Z. Yu, M. Cao, S. Zhang, M. T. Lanagan, H. Liu, *Adv. Mater.* **2017**, *29*, 29.

[14] K. Y. Lau, A. S. Vaughan, G. Chen, *IEEE Electr. Insul. Mag.* **2015**, *31*, 45.

[15] H. Li, F. Liu, B. Fan, D. Ai, Z. Peng, Q. Wang, *Small Methods* **2018**, *2*, 1700399.

[16] M. Guo, J. Jiang, Z. Shen, Y. Lin, C.-W. Nan, Y. Shen, *Mater. Today* **2019**, *29*, 49.

[17] S. X. Drakopoulos, J. Karger-Kocsis, Á. Kmetty, L. Lendvai, G. C. Psarras, *Carbohydr. Polym.* **2017**, *157*, 711.

[18] K. Lau, A. Vaughan, G. Chen, I. Hosier, A. Holt, K. Ching, *IEEE Trans. Dielectr. Electr. Insul.* **2014**, *21*, 340.

[19] B. Li, E. Manias, *MRS Adv.* **2017**, *2*, 357.

[20] B. Li, F. Salcedo-Galan, P. I. Xidas, E. Manias, *ACS Appl. Nano Mater.* **2018**, *1*, 4401.

[21] V. Tomer, G. Polizos, C. A. Randall, E. Manias, *J. Appl. Phys.* **2011**, *109*, 074113.

[22] B. Li, P. I. Xidas, E. Manias, *ACS Appl. Nano Mater.* **2018**, *1*, 3520.

[23] I. Rytöluoto, A. Gitsas, S. Pasanen, K. Lahti, *Eur. Polym. J.* **2017**, *95*, 606.

[24] A. Kahouli, O. Gallot-Lavallée, P. Rain, O. Lesaint, L. Heux, C. Guillermin, J.-M. Lupin, *J. Appl. Polym. Sci.* **2015**, *132*, 42602.

[25] G. M. Tsangaris, G. C. Psarras, N. Kouloumbi, *J. Mater. Sci.* **1998**, *33*, 2027.

[26] O. Vryonis, S. T. H. Virtanen, T. Andritsch, A. S. Vaughan, P. L. Lewin, *J. Mater. Sci.* **2019**, *54*, 3035.

[27] Z.-M. Dang, J.-K. Yuan, S.-H. Yao, R.-J. Liao, *Adv. Mater.* **2013**, *25*, 6334.

[28] T. Hanemann, D. V. Szabó, *Materials* **2010**, *3*, 3468.

[29] P. Kim, S. C. Jones, P. J. Hotchkiss, J. N. Haddock, B. Kippelen, S. R. Marder, J. W. Perry, *Adv. Mater.* **2007**, *19*, 1001.

[30] G. C. Manika, G. C. Psarras, *Express Polym. Lett.* **2019**, *13*, 749.

[31] Q. Li, L. Chen, M. R. Gadinski, S. Zhang, G. Zhang, H. Li, A. Haque, L. Q. Chen, T. Jackson, Q. Wang, *Nature* **2015**, *523*, 576.

[32] Q. Li, G. Zhang, F. Liu, K. Han, M. R. Gadinski, C. Xiong, Q. Wang, *Energy Environ. Sci.* **2015**, *8*, 922.

[33] V. Georgakilas, J. N. Tiwari, K. C. Kemp, J. A. Perman, A. B. Bourlinos, K. S. Kim, R. Zboril, *Chem. Rev.* **2016**, *116*, 5464.

[34] I. Kovalenko, D. G. Bucknall, G. Yushin, *Adv. Funct. Mater.* **2010**, *20*, 3979.

[35] P. Gonon, A. Boudefel, *J. Appl. Phys.* **2006**, *99*, 024308.

[36] L. A. Fredin, Z. Li, M. T. Lanagan, M. A. Ratner, T. Marks, *J. Adv. Funct. Mater.* **2013**, *23*, 3560.

[37] C. L. Choy, *Polymer* **1977**, *18*, 984.

[38] E. C. Senis, I. O. Golosnoy, J. M. Dulieu-Barton, O. T. Thomsen, *J. Mater. Sci.* **2019**, *54*, 8955.

[39] S. Rastogi, D. R. Lippits, G. W. M. Peters, R. Graf, Y. Yao, H. W. Spiess, *Nat. Mater.* **2005**, *4*, 635.

[40] P. Selg, H. H. Brintzinger, R. A. Andersen, I. T. Horváth, *Angew. Chemie Int. Ed.* **1995**, *34*, 791.

[41] S. X. Drakopoulos, G. Forte, S. Ronca, *Ind. Eng. Chem. Res.* **2020**, *59*, 4515.

[42] S. Rastogi, Y. Yao, S. Ronca, J. Bos, J. Van Der Eem, *Macromolecules* **2011**, *44*, 5558.

[43] S. Ronca, T. Igarashi, G. Forte, S. Rastogi, *Polymers* **2017**, *123*, 203.

[44] A. B. Robbins, S. X. Drakopoulos, I. Martin-Fabiani, S. Ronca, A. Minnich, *J. Proc. Natl. Acad. Sci.* **2019**, *116*, 17163.

[45] S. X. Drakopoulos, S. Ronca, I. Martin-Fabiani, in *Crystallization as Studied by Broadband Dielectric Spectroscopy* (Eds: T. A. Ezquerra, A. Nogales), Springer, Cham **2020**, p. 243.

[46] H. Fischer, P.; Nissen, K, *IEEE Trans. Electr. Insul.* **1976**, *11*, 37.

[47] S. X. Drakopoulos, O. Tarallo, L. Guan, I. Martin-Fabiani, S. Ronca, *Molecules* **2020**, *25*, 3225.

[48] A. Pucci, N. Tirelli, E. A. Willneff, S. L. M. Schroeder, F. Galembeck, G. Ruggeri, *J. Mater. Chem.* **2004**, *14*, 3495.

[49] D. Bitounis, J. Pourchez, V. Forest, D. Boudard, M. Cottier, J. P. Klein, *Biomaterials* **2016**, *76*, 302.

[50] S. X. Drakopoulos, G. C. Psarras, S. Ronca, *Express Polym. Lett.* **2021**, *15*, 492.

[51] G. Forte, S. Ronca, *Int. J. Polym. Sci.* **2017**, *2017*, 2017.

[52] S. X. Drakopoulos, G. C. Psarras, G. Forte, I. Martin-Fabiani, S. Ronca, *Polymer* **2018**, *150*, 35.

[53] P. Frübing, D. Blischke, R. Gerhard-Multhaupt, M. Salah Khalil, *J. Phys. D: Appl. Phys.* **2001**, *34*, 3051.

[54] S. Ronca, G. Forte, H. Tjaden, S. Rastogi, *Ind. Eng. Chem. Res.* **2015**, *54*, 7373.

[55] J. Lu, K.-S. Moon, J. Xu, C. P. Wong, *J. Mater. Chem.* **2006**, *16*, 1543.

[56] J. A. Johnson, A. A. Maznev, J. Cuffe, J. K. Eliason, A. J. Minnich, T. Kehoe, C. M. S. Torres, G. Chen, K. A. Nelson, *Phys. Rev. Lett.* **2013**, *110*, 1.

[57] N. K. Ravichandran, H. Zhang, A. Minnich, *J. Phys. Rev. X* **2018**, *8*, 41004.

[58] G. C. Manika, G. C. Psarras, *High Volt.* **2016**, *1*, 151.

[59] J.-T. Yeh, S.-C. Lin, C.-W. Tu, K.-H. Hsie, F.-C. Chang, *J. Mater. Sci.* **2008**, *43*, 4892.

[60] A. Linares, J. C. Canalda, M. E. Cagiao, M. C. Garcia-Gutiérrez, A. Nogales, I. Martín-Gullón, J. Vera, T. A. Ezquerra, *Macromolecules* **2008**, *41*, 7090.

[61] M. Azuma, L. Ma, C. He, T. Suzuki, Y. Bin, H. Kurosu, M. Matsuo, *Polymer* **2004**, *45*, 409.

[62] Y. Li, J. Moll, L. S. Schadler, H. Liu, S. K. Kumar, A. Z. Panagiotopoulos, J. Ilavsky, B. C. Benicewicz, V. Pryamitsyn, V. Ganesan, J. F. Douglas, R. H. Colby, D. Acehan, P. Thiyagarajan, P. Akcora, *Nat. Mater.* **2009**, *8*, 354.

[63] M. J. Gall, P. J. Hendra, O. J. Peacock, M. E. A. Cudby, H. A. Willis, *Spectrochim. Acta Part A Mol. Spectrosc.* **1972**, *28*, 1485.

[64] S. Abbate, M. Gussoni, G. Zerbi, *J. Chem. Phys.* **1980**, *73*, 4680.

[65] M. Pigeon, R. E. Prud'homme, M. Pezolet, *Macromolecules* **1991**, *24*, 5687.

[66] G. R. Strobl, W. Hagedorn, *J. Polym. Sci. Polym. Phys. Ed.* **1978**, *16*, 1181.

[67] F. J. Boerio, J. L. Koenig, *J. Chem. Phys.* **1970**, *52*, 3425.

[68] T. J. Norman, C. D. Grant, D. Magana, J. Z. Zhang, J. Liu, D. Cao, F. Bridges, A. Van Buuren, *J. Phys. Chem. B* **2002**, *106*, 7005.

[69] S. Watanabe, J. Dybal, K. Tashiro, Y. Ozaki, *Polymer* **2006**, *47*, 2010.

[70] M. Watari, H. Higashiyama, N. Mitsui, M. Tomo, Y. Ozaki, *Appl. Spectrosc.* **2004**, *58*, 248.

[71] H. Shinzawa, W. Kanematsu, I. Noda, *Vib. Spectrosc.* **2014**, *70*, 53.

[72] B. Koo, P. Goli, A. V. Sumant, P. C. Dos Santos Claro, T. Rajh, C. S. Johnson, A. A. Balandin, E. V. Shevchenko, *ACS Nano* **2014**, *8*, 7202.

[73] T. A. Ezquerra, J. C. Canalda, A. Sanz, A. Linares, *Colloid Polym. Sci.* **2014**, *292*, 1989.

SUPPORTING INFORMATION

Additional supporting information may be found online in the Supporting Information section at the end of this article.